

# Measurements of Directional Sea Surface Waves near Sakhalin Island by Array of Bottom Stations

A. V. Kokorina<sup>a, \*</sup>, A. V. Slunyaev<sup>a, b, c</sup>, A. I. Zaitsev<sup>a, d</sup>, and R. V. Leonenkov<sup>d</sup>

<sup>a</sup> *Gaponov-Grekhov Institute of Applied Physics, Russian Academy of Sciences, Nizhny Novgorod, 603950 Russia*

<sup>b</sup> *Higher School of Economics, National Research University, Nizhny Novgorod, 603155 Russia*

<sup>c</sup> *Il'ichev Pacific Oceanological Institute, Far East Branch, Russian Academy of Sciences, Vladivostok, 690041 Russia*

<sup>d</sup> *Special Research Bureau for Automation of Marine Researches, Far East Branch, Russian Academy of Sciences, Yuzhno-Sakhalinsk, 693023 Russia*

\**e-mail: a.sergeeva@ipfran.ru*

Received April 19, 2024; revised July 27, 2024; accepted September 2, 2024

**Abstract**—Field measurements of sea waves have been carried out off the coast of Sakhalin Island using an array of three bottom pressure sensors. The stability of statistical characteristics estimated by independent devices comprised in the array has been analyzed. The probability distribution of wave heights qualitatively corresponds to the Glukhovsky distribution but exhibits a lower probability of high wave occurrence. The spatiotemporal spectra of waves are reconstructed. It is shown that the angular distribution of the spectral density of waves over two days of measurements is well described by the theoretical cosine squared distribution, and its width varies in the range of  $50^\circ$ – $90^\circ$ . The dominant direction of wave propagation is from the northeast. An independent method is proposed for estimating the local water depth by data from the array.

**Keywords:** sea surface waves, field measurements, bottom pressure, data processing, directional wave spectra, angular distribution of spectral density

**DOI:** 10.1134/S000143382470066X

## INTRODUCTION

The importance of problems of adequate description of wind waves, including the dynamic and probabilistic aspects, estimates of maximum possible waves and frequency of their repeatability, understanding of the laws of generation, development, and propagation of wind waves, is out of question. The already existing models are steadily developed with allowance for better physical understanding and improvement of the mathematical and computational apparatus; they are reviewed with involvement of new laboratory and field data.

The Special Research Bureau for Automation of Marine Researches, Far East Branch, Russian Academy of Sciences, for the last approximately 15 years carries out instrumental measurements of sea waves near the coast of Sakhalin Island by recording variations in bottom pressure. The measurement campaigns were implemented with installation of one or several autonomous sensors for a period of up to six months. The results of processing of measurements for different years were presented in (Zaitsev et al., 2011; Kuznetsov et al., 2014; Didenkulova and Zaitsev, 2019; Kokorina et al., 2022; Slunyaev et al., 2023a). Main attention is paid to ranges of characteristics of the recorded waves (periods, heights), extreme waves

(frequency of appearance, maximum amplifications, shape), probability distributions of waves, including anomalously high waves (rogue waves). In particular, in a recent work (Slunyaev et al., 2023a), the measurement data were transformed to dimensionless characteristics for better correspondence with acting physical mechanisms. In addition, large variability of physical conditions of measurement at only one point of wave detection (related, in particular, to the change in wave periods) and adequacy of the Glukhovsky distribution for describing the probability distribution of heights of nonlinear waves were shown for a considerable part of the measurements.

The obtained data of full-scale records are of great interest in the aspect of verifying the extreme wave pattern obtained by results of direct numerical simulation (for example, (Slunyaev and Kokorina, 2020)). Numerical simulation of the evolution of irregular waves within the framework of dynamic equations of hydrodynamics (Monte Carlo simulation) is used as a more careful but laborious alternative to the calculation of kinetic equations (see the review (Slunyaev et al., 2023b)). The latter use a number of approximations (first of all, assumptions about randomness and non-correlatedness of waves and slowness of the nonlinear evolution), which makes it impossible to describe rap-

idly developing nonlinear processes associated most of all with the phenomenon of rogue waves. Wave conditions are described using parametric frequency spectra  $S(\omega)$ , e.g., the Pierson–Moskowitz spectrum or JONSWAP (Massel, 1996; Holthuijsen, 2007; Lopatukhin, 2012). Since the primitive hydrodynamics equations are solved for time derivatives, the solution of the initial problem is the most natural. Then, to specify the initial conditions, the frequency spectrum should be transformed into the spectrum of wave vectors  $S(\mathbf{k})$ . This usually presupposes factorization of the directional wave spectrum of the form  $S(\mathbf{k}) = S(k)D(\theta)$ , where  $k = |\mathbf{k}|$  is the modulus of the wave vector and  $\theta$  is its corresponding angle in the horizontal plane for a certain model directional distribution function  $D(\theta)$ . We carry out such calculations for conditions of a large and finite depth (Slunyaev and Kokorina, 2020; Slunyaev, 2023); they are also actively carried out by other research groups, e.g., (Xiao et al., 2013; Ducroz et al., 2016; Kirezci et al., 2021; Wang et al., 2021; Chalikov, 2023).

Information about angular spectra of waves is important both for interpreting measurement data at a single spatial point (in particular, extraction of wave systems that mix in the frequency spectrum) and for estimating dynamic and probabilistic properties of wind waves. It is known that conditions of crossed wave breaking considerably differ from those for unidirectional waves (Babanin, 2011); the picture of nonlinear wave interactions depends heavily on the angular distribution, including the dependence of conditions of modulational instability of waves the development of which leads to extremization of waves (Onorato et al., 2009).

An array of three synchronized bottom pressure sensors was installed in October 2022 in Mordvinova Bay especially to acquire data about angular distribution of wind waves. Using systems of spaced string wave recorders is a standard way of measuring directional waves on the sea surface (e.g., (Davidan et al., 1978; Young, 1994; Donelan et al., 1996)). Distributed systems of bottom pressure stations were also used for tracking the wave propagation, e.g., (Squire et al., 2021). When using bottom pressure recorders, information about the directional wave spectrum is usually acquired by additional measurements (for example, fields of flows), see (Montoya and Dally, 2016). The measurement of angular spectra of waves based only on data on pressure variations near the bottom was carried out near the Atlantic coast of North Carolina (Currituck Spit, United States) during about 23 years (Long and Oltman-Shay, 1991; Long, 1994). The system consisted of nine devices placed on one line with a total length of more than 200 m along the 8-m isobath and the tenth sensor shifted by 5 m towards the sea. The devices were placed at different distances from each other, optimally for using the iterative maximum likelihood estimator method for reconstructing the angular spectrum. The devices were powered by

cable. Apparently, arrays of bottom pressure sensors were not used previously in Russian water basins for records of directional waves of the wind range.

In this work, results of bottom pressure records from an array of three sensors during one month are processed. These data are used both to determine capability of this measurement scheme, including cross-validation of instrumental data from different sensors, and to reconstruct spatial spectra of directional waves, including the estimate of typical widths of angular spectra and profiles of their distributions required in problems of direct numerical simulation of irregular sea waves. Also, probabilistic properties of the measured waves under conditions of intense and weak waves are analyzed. It is discussed that the presence of simultaneous information about the spatial and frequency spectra can be used for independent estimation of the measurement point depth.

## 1. CONDITIONS OF THE FIELD EXPERIMENT AND INSTRUMENTAL DATA

An array of three energy-independent pressure sensors rigidly fixed on a metal frame was installed on the bottom in Mordvinova Bay of the Sea of Okhotsk near the eastern coast of the southern part of Sakhalin Island (Fig. 1) on October 19 and raised on November 24, 2022. The bay is open for the entry of waves from the east from the Sea of Okhotsk. The region is separated from the Pacific by the Kuril Ridge. The sea bottom drops to the 100-m mark with the distance of more than 20 km from the shore. The array was not far from the Krasnoarmeiskaya branch connecting the Tunaicha lake-like lagoon with the sea. According to data of previous measurement campaigns, water salinity at the installation place lies within 32–33 PSU and varies insignificantly.

The array is an equilateral triangle with a side length  $\Delta l = 1.5$  m at the vertices of which there are independent sensors (see the scheme in Fig. 2) based on Microtensor D 0.25-T temperature-compensated piezoconverters of excessive pressure with a resolving capacity of 0.01% in a pressure range from 0 to 0.25 MPa. The sensors were calibrated before and after the experiment; they were synchronized before the immersion. The array was installed horizontally at a depth of about 11.5 m. The estimate of the difference between actual sensor depths according to the obtained data was about 1%. The side with the sensors A and B is elongated from south to north; the sensor C is oriented to the east. The initial measurement data used for the analysis are about 800 h of continuous records of pressure  $P(t)$  with a frequency of 8 Hz, from October 20 to November 23.

The total pressure measured by bottom sensors is composed of hydrodynamic pressure and air column pressure,  $P(t) = P_{\text{hyd}}(t) + P_{\text{atm}}(t)$ . Variations in the hydrodynamic pressure are caused by passage of waves

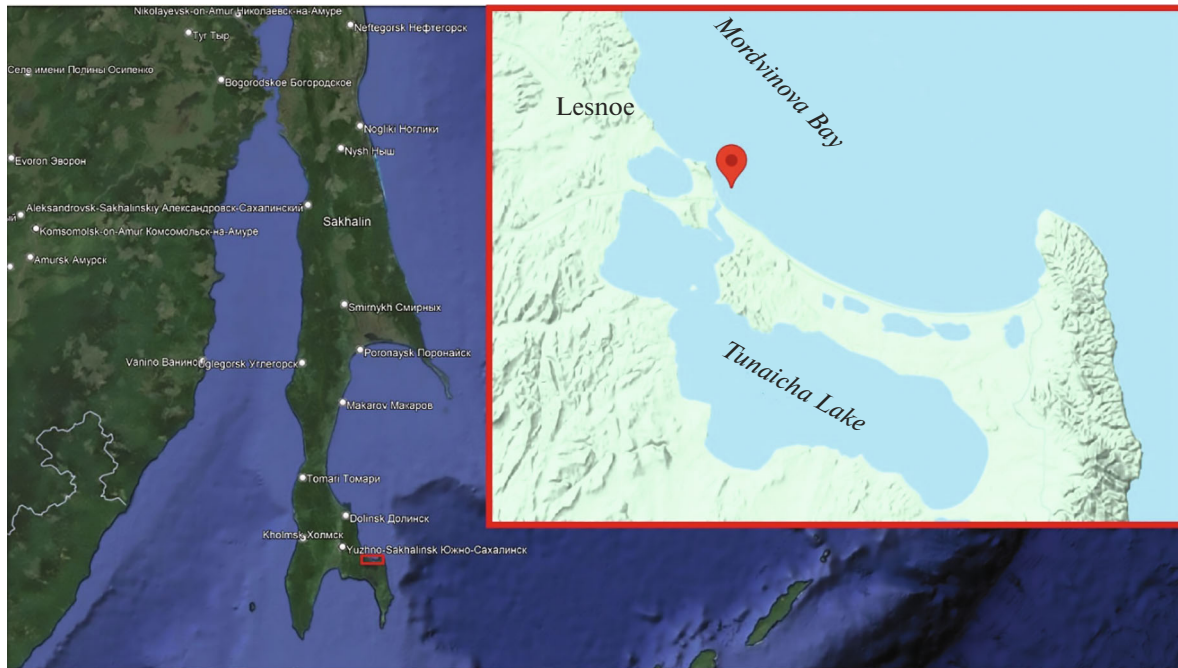


Fig. 1. Place of measurements ( $46^{\circ}51'50.26''$  N,  $143^{\circ}10'30''$  E).

with different lengths and heights. The atmospheric pressure component  $P_{\text{atm}}$  is taken to be constant at the time of array immersion. The initial data  $P(t)$  were processed using a low-frequency filter eliminating all variations with periods of more than 10 min which are associated with intense variations in atmospheric pressure, tidal, driven effects, etc. The record from sensor A after filtering is shown in Fig. 3. Following the standard procedure, long records from the sensors were divided into nonintersecting intervals of 20 min each which are assumed to be statistically homogeneous. For each of the 20-min samples, the point depth  $h$  was determined in terms of the hydrostatic formula for the mean determined for the considered time interval by the initial nonfiltered series:  $h = \langle P_{\text{hyd}} \rangle / (\rho g)$ , where  $\rho = 1023 \text{ kg/m}^3$  and  $g = 9.81 \text{ m/s}^2$  is the water density and acceleration of gravity, respectively. Ignoring possible long-term variations in atmospheric pressure leads to an error in the depth estimate. For a realistic pressure drop of 175 mm Hg, the equivalent height of a water column is up to impressive 2.4 m. However, in the interval of dates of measurements, the spread of atmospheric pressure was only 19 mm Hg (Weather-Archive.ru), which provides the error in the estimate of the depth of not more than 26 cm. The depth averaged over the whole time of measurements was 11.5 m; we treat it as a conventional depth of the point of array installation. Variations in depths  $h$  in the measured data with respect to this average value reach 2 m. The corresponding range of values of the dimensionless depth parameter  $kh$  (here,  $k$  is the wavenumber determined for each 20-min sample by the characteristic

period of waves in accordance with the dispersion relation, as it is discussed in Section 2) turns out to be rather wide, from 0.5 to 1.7. Therefore, the discussed measurements carried out at a single point in fact correspond to conditions from shallow to relatively deep water.

In this work, filtered data on pressure  $P_{\text{hyd, filt}}(t)$  are recalculated to the displacement of the sea surface over the measurement point  $\eta(t)$  using the hydrostatic theory, by analogy with the previous works (Zaitsev et al., 2011; Kuznetsov et al., 2014; Kokorina et al., 2022;

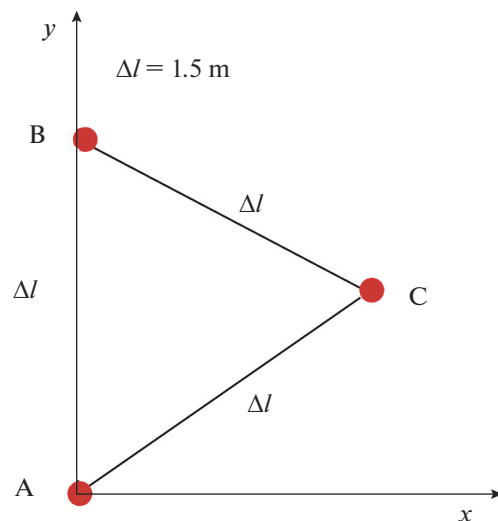
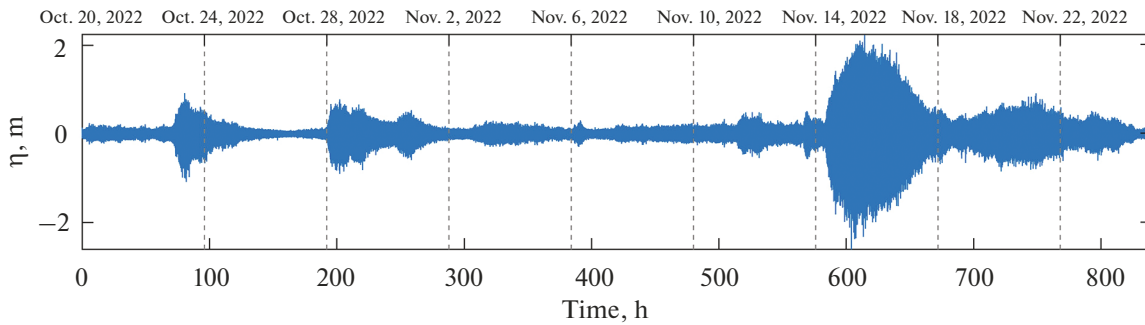


Fig. 2. Scheme of the array of three sensors. The  $Ox$  axis is directed to the east; the  $Oy$  axis, to the north.



**Fig. 3.** Record of the surface displacement after filtering of long waves. Here and below, the labels on the top correspond to beginning of days; on the bottom, the time relative to the conventional time of the beginning of measurements in hours.

Slunyaev et al., 2023a):  $\eta(t) = P_{\text{hyd, filt}}(t)/(\rho g)$ . It can be applied only under conditions of shallow water and linearity of waves, which is by no means always the case for the measurements under discussion. The effects of deviation from the hydrostatic theory are neglected in this work. For this reason, one may believe with a great deal of rigor that the investigation carried out below concerns records of bottom pressure.

## 2. GENERAL PICTURE OF CHARACTERISTICS OF MEASURED WAVES

As described above, the instrumental data series was divided into a sequence of 20-min zero mean record segments of the surface displacement,  $\langle \eta \rangle = 0$ . For each of the intervals, averaged values of characteristics were determined: the standard deviation  $\sigma$  and the significant height  $H_s = 4\sigma$  related to it; the fourth central statistical moment for the surface displacement  $m_4 = \langle \eta^4 \rangle / \sigma^4 - 3$  (the kurtosis); the mean period of waves after crossing the zero level  $T_z$ ; and others. The evolution of the aforesaid quantities during the measurements is presented in Fig. 4. Since the measurements were carried out simultaneously by three sensors placed at a short distance from each other (as compared to the wavelength), the values used are averaged over three sensors (the black line); the light green symbols in Fig. 4 represent values of the corresponding parameter for each of the three sensors.

Their significant height (Fig. 4a, the black line) for the whole measurement period was about 20 cm on the average (see the diagram of the condition implementation frequency in the right-hand part of the figure). One may distinguish three intervals in which the intense wave was recorded; their beginnings correspond approximately to times  $t = 80, 200,$  and  $600$  h from the conventional time of the measurement start in the midnight of October 20 (see the scale above the figure). According to meteorological data for Yuzhno-Sakhalinsk (WeatherArchive.ru), they correspond to heavier winds of up to 3 m/s on October 22–23, to 4 m/s on October 28–29, and to 7 m/s on November

13 (i.e., two or three days before the observed maximum of the significant height). The first two cases are characterized by the rapid increase in  $H_s$  to a value of about 1 m and further slow decrease to the background value. The last episode is relatively long; the significant wave height reached 3 m and the maximum height by the estimate of the surface displacement reconstruction was  $H = 4.3$  m. According to surface weather maps of the Japan Meteorological Agency, a cyclone passed on November 12–14 south of the island from west to east with a wind speed of up to 35 knots (65 km/h).

Values of the fourth statistical moment  $m_4$  in the sequence of 20-min samples are constructed in Fig. 4a by red symbols for all three sensors in the same axes as the significant height  $H_s$ ; however, they are dimensionless quantities. In most cases, values of the kurtosis are close to zero corresponding to a random Gaussian process but distributed around this value rather widely, see the diagram in the right-hand part of the figure. Values  $m_4 = 1$  and larger are not infrequent, which should correspond to higher probability of high waves as compared to normal statistic. The average value of  $m_4$  is a little less than zero. It is clearly seen that values of  $m_4$  in the storm period move below zero, i.e., the probability of the appearance of big waves as compared to  $H_s$  significantly decreases. In the data presented, large values of the kurtosis are implemented under conditions of waves with a small significant height.

Periods of waves  $T_z$  were determined by two methods: up zero-crossing and down zero-crossing as applied to time series. Both methods yielded very close estimates of wave periods; for this reason, Fig. 4b presents results of only one of them (up zero-crossing). As judged by the figure, the initial moments of all three time intervals of intense wave recording correspond to conditions of relatively short waves with periods of less than 6 s which then became longer. In general, characteristic periods of waves varied in the range of 6–14 s, partly sharply, leading to significant changes in the parameter of the local dimensionless depth from  $kh = 0.5$  to  $kh = 1.7$ , as is shown in Fig. 4c (we recall that the estimate of long-period changes in the depth

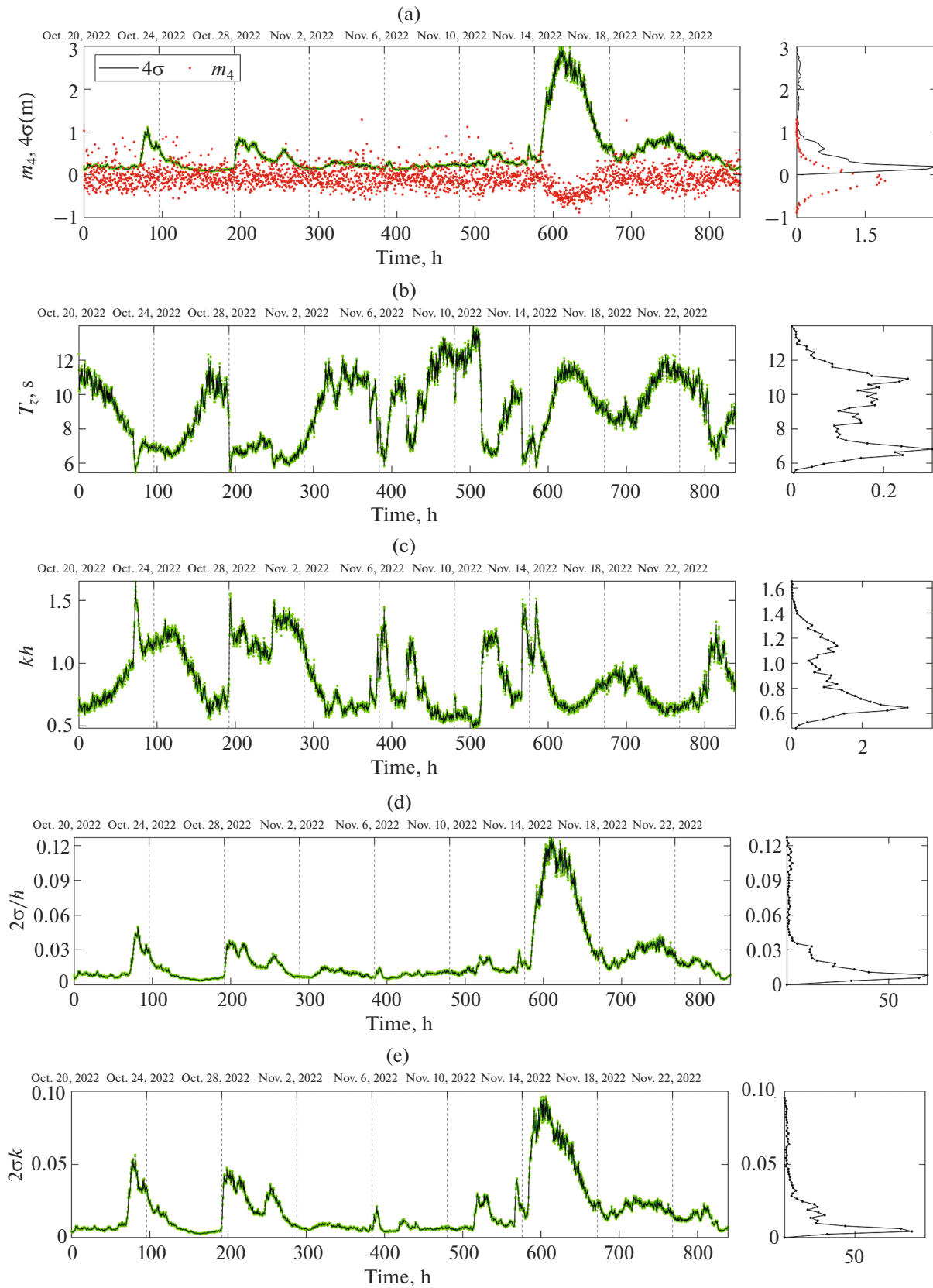


**Fig. 4.** Variation in wave parameters in time: (a) significant height  $4\sigma$  and kurtosis  $m_4$ ; (b) period  $T_z$ ; (c) dimensionless depth parameter  $kh$ ; (d) shallow-water nonlinearity parameter  $2\sigma/k$ ; and (e) steepness  $2\sigma k$ . The green dots form values from different sensors; the black line is the result of averaging over the sensors. In the diagrams to the right, the probability density functions of the corresponding quantities are constructed.

$h$  is only about 20%). Here, the wavenumber  $k$  is calculated in terms of the dispersion relation for waves at the depth  $h$ , reverting the theoretical formula of  $\omega(k)$  for the cyclic frequency  $\omega = 2\pi/T_z$ :

$$\omega = \sqrt{gk \tanh(kh)}. \quad (1)$$

The storm waves recorded in the middle of November corresponded to conditions of shallow water  $kh \approx 0.6$ , as the major part of recorded waves, see the diagram in the right-hand part of Fig. 4c. The second peak of the most probable conditions in the diagram corresponds to the dimensionless depth parameter  $kh \approx 1.2$ . The conditions of relatively deep water  $kh > 1.4$  were implemented during a short time.

Two estimates of wave nonlinearity are constructed in Figs. 4d and 4e: the first one is defined as the ratio of half the significant height to the depth  $H_s/(2h)$ ; the second one is the estimate of the mean steepness of waves  $kH_s/2$ . The ‘‘shallow’’ nonlinearity of waves during a storm reaches the value  $H_s/(2h) = 0.12$ ; the maximum steepness, slightly less than  $kH_s/2 = 0.1$ . These estimates correspond to conditions long before the threshold of regular wave breaking (Holthuijsen, 2007). The constructed distributions qualitatively resemble data for  $H_s$  (Fig. 4a); however, the sequence in Fig. 4e exhibits, in particular, periods of records of steep waves weakly discerned in Figs. 4a and 4d. In addition, one may note in Fig. 4e a stronger skewness of data for the storm interval: the peak in the record of the steepest waves is before the peak of the most intense waves (with respect to the parameter  $H_s$  of the ratio of the wave amplitude to the depth  $H_s/(2h)$ ).

In our works (Kokorina et al., 2022, Slunyaev et al., 2023a), based on analysis of data of wave measurements near Sakhalin Island, it was shown that the probability distributions of intense wave heights ( $H > H_s$ ) were well described by the theoretical Glukhovsky distribution

$$P_G(H) = \exp \left[ -\frac{\pi}{4 \left(1 + \frac{n}{\sqrt{2\pi}}\right)} \left(\frac{H}{\bar{H}}\right)^{\frac{2}{1-n}} \right], \quad n = \frac{\bar{H}}{h}, \quad (2)$$

which takes into account the finite depth effect in terms of the nonlinearity parameter  $n$ ; the fraction of high waves decreases at a greater degree of nonlinearity. The quantity  $\bar{H} = \sqrt{2\pi}\sigma$  in formula (2) is the mean height of waves. In the large depth limit  $n \rightarrow 0$ , dependence (2) is transformed into the Rayleigh distribution. The behavior of the kurtosis in Fig. 4a agrees with these conclusions: the maximum value of nonlinearity falls on the storm period and the kurtosis at this time undergoes a noticeable decrease.

In Fig. 5, probability distributions for the abnormal wave height  $H$  according to measurements from the array and the theoretical Rayleigh and Glukhovsky distributions are constructed. The method of deter-

mining the wave height (up or down zero-crossing) has no effect on the result in this case. The theoretical dependences were constructed using the definition of the significant height as the mean of one third of maximally high waves in the sample,  $H_{1/3}$ , similarly to (Slunyaev et al., 2023a); in the limit of waves with the Gaussian statistic with a narrow spectrum,  $H_{1/3} \approx 4.004\sigma$  and  $\bar{H} = \sqrt{2\pi}H_{1/3}/4$  (Massel, 1996). In Fig. 5a, the probability distribution is constructed for the whole measurement period. The heights were normalized to local values of  $H_{1/3}$  in each 20-min sample; the nonlinearity parameter  $n$  in the Glukhovsky distribution (2) was calculated in terms of averaged values of the local significant height and local depth. In contrast to result of the analysis of longer measurements in (Kokorina et al., 2022; Slunyaev et al., 2023a), the experimental curve constructed by data from the array does not coincide with the Glukhovsky distribution; it is located in the region  $H/H_{1/3} > 1$ , considerably lower than the theoretical distribution. For  $H/H_{1/3} < 1$ , the experimental curve is above the theoretical one, which was also mentioned in (Kokorina et al., 2022).

Figure 5b presents the probability distributions constructed by data of three samples composed by the condition on the magnitude of the significant height: less than 0.5 m, from 0.5 to 1 m, and more than 1 m. The experimental distributions for two samples of low-rise waves almost coincided, while the distribution for  $H_{1/3} \geq 1$  m (in fact, for storm waves in the middle of November) exhibits a significant difference: the probability of waves that are high as compared to  $H_{1/3}$  considerably decreases for it, and the probability of waves with a low height (on the order of  $0.5 H_{1/3}$ ) increases. The decrease in the probability of the appearance of high waves during the recorded storm agrees with the behavior of the kurtosis in Fig. 4a. Such change in the probability distribution for nonlinear waves at a shallow depth qualitatively corresponds to the Glukhovsky distribution discussed above. In Fig. 5b, Glukhovsky distributions (2) are constructed with filling in different colors for the same three ranges of  $H_{1/3}$ . It is seen that the experimental data in the region of waves that are large as compared to  $H_{1/3}$  are significantly lower than the theoretical prediction, as in the case of the distribution for the whole measurement period in Fig. 5a. Using measurement data selection on the basis of magnitude of the nonlinear parameter  $H_{1/3}/(2h)$  yielded a similar result. Thus, for data from the array, no quantitative coincidence with the Glukhovsky distribution was found.

### 3. COMPARISON OF DATA FROM THREE SENSORS OF THE ARRAY

Since the distance between the sensors is small as compared to the characteristic wavelength (for the maximum value of the dimensionless depth  $kh = 1.7$

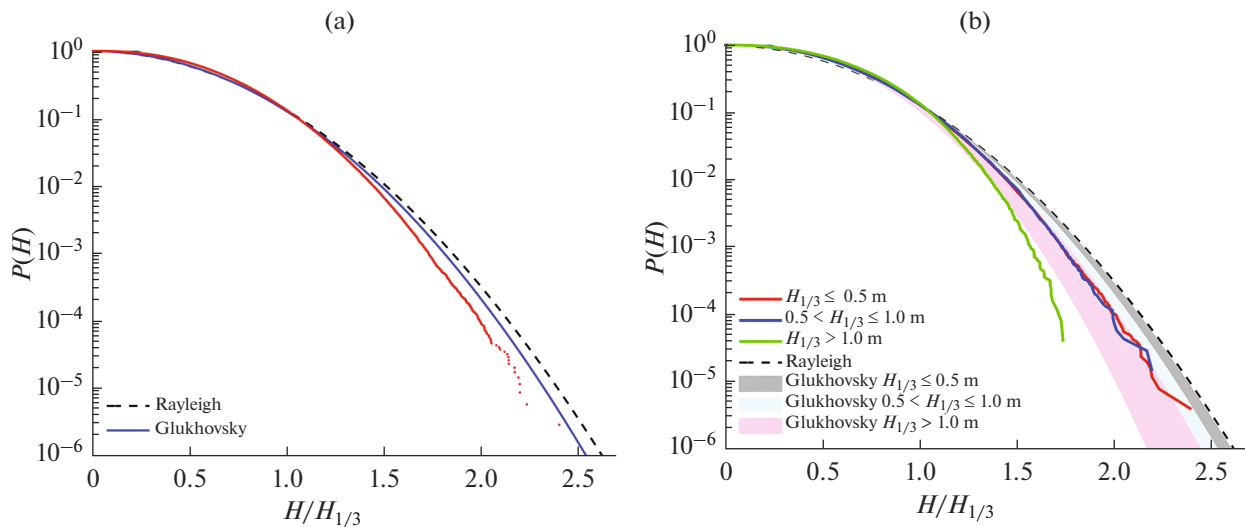


**Fig. 5.** Exceedance probability distribution of wave height  $H$  (a) over all measurement data and (b) for three ranges of  $H_{1/3}$  (the thick lines). Glukhovsky distributions (2) in panel (b) are constructed by filling for the corresponding ranges of  $H_{1/3}$ . The theoretical Rayleigh distribution is constructed by the dashed line.

and mean estimate of the place depth  $h = 11.5$  m, the wavelength is greater than 40 m), one may assume for the statistical estimates that they record the same sequence of waves. Three equivalent records can be used for estimating the accuracy of measurements and stability of the data averaging result from each of the devices. The spread of values of key parameters in results from different sensors comprised in the array can be seen in Fig. 4—by the degree of the deviation of green symbols from the mean value over the sensors constructed by the black line.

The spread of root-mean-square shifts  $\sigma$  by data from three devices relative to their mean value is presented in Fig. 6a. Each point in the plot reflects the relative deviation of the value for one of the devices (by different colors) from the mean in a 20-min sample. One can see systematic discrepancy by  $\sim 2\%$  in the first approximately ten days of measurements; then, the discrepancy becomes less regular and by the end of the month seems to be fully chaotic within limits of 10%, with the largest deviations corresponding to sensor B.

One may assume that the high statistical moment—the kurtosis—should be the most sensitive to the appearance of extreme values among the probabilistic characteristics under consideration. The spread of kurtosis values  $m_4$  in 20-min samples is constructed in Fig. 6b. It is seen that the variability in the first days is minimum and can be estimated as 2–3%. The spread increases with time; after 500 h of measurements, it becomes somewhat greater than 10%. Note that the arrival of very high waves in the storm period of 600–650 h does not lead to any noticeable increase in the spread of values of  $m_4$ .

The experimental probability distributions constructed in Fig. 5 for three different sensors almost coincide.

To reconstruct the propagation direction of waves and their spatial spectrum, it is important to synchronize the measuring devices. The actual synchronicity of the measurements was checked by tracking the behavior of the maximum of the correlation function  $R_{mn}(\tau)$  in time

$$R_{mn}(\tau) = \frac{\int_{\tau} \eta_m(t) \eta_n(t - \tau) dt}{\sqrt{\int_{\tau} \eta_m^2(t) dt} \sqrt{\int_{\tau} \eta_n^2(t) dt}} \quad (3)$$

for a pair of data series  $\eta_m(t)$  and  $\eta_n(t)$  from sensors  $m$  and  $n$ . Here, integration over intervals of 20 min was performed by summation of corresponding discrete values; delays  $\tau$  were chosen with the same discretization.

An example of the behavior of the correlation function in the region near its maximum for sensors A and B in the first three days is shown in Fig. 7, where the color corresponds to values of  $R(\tau)$ . One can see considerable (on the order of a second) instantaneous shifts of maximums of the correlation function. They began after 48 h of measurements and turned out to be problems of technical character (missed measurement instants). Comparison of data obtained from sensors A and C did not reveal such synchronization errors, suggesting that only the device B turned out to be dysfunctional. At a later stage, desynchronization of sensor B increases and has a less regular character, which makes it impossible to use data from the array for constructing spatial spectra of waves. That is why only the measurements for the first two days are used for this purpose. It is evident that accumulation of the relative shift of time series from different sensors makes a contribution to the difference of estimates of wave characteristics by data from three devices and can explain the increase in the spread of values observed in Fig. 6.

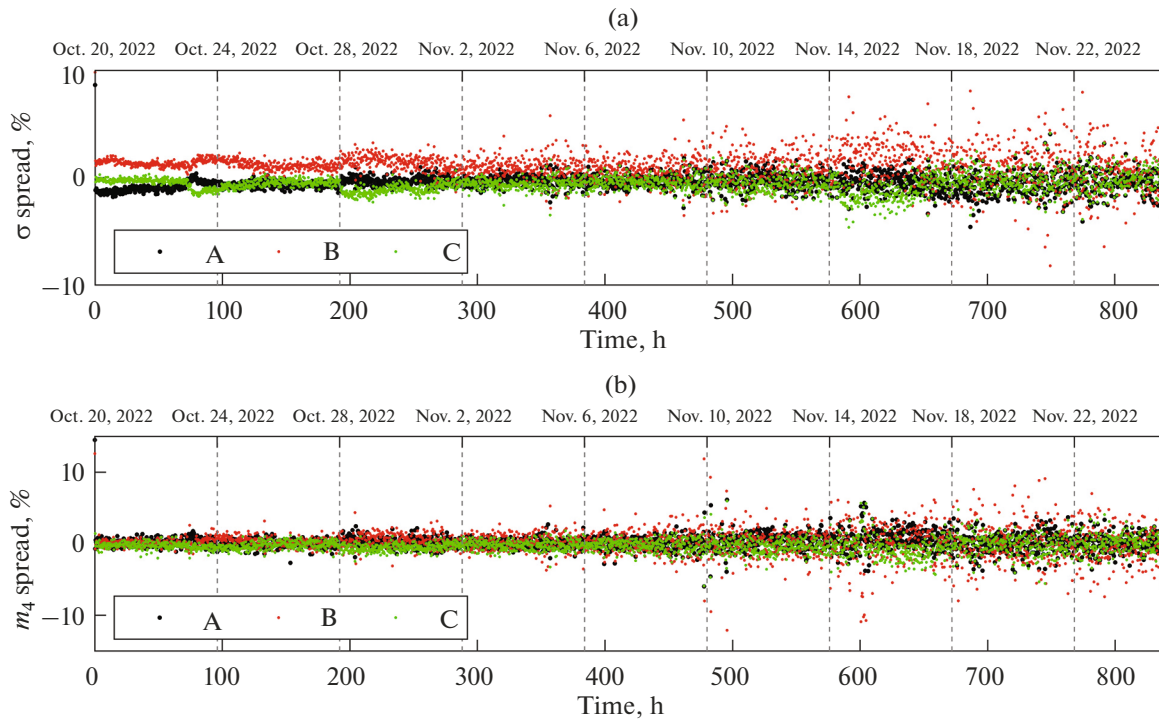


Fig. 6. Spread of values of the (a) standard deviation and (b) kurtosis  $m_4$  according to measurements from three sensors relative to the mean over the sensors.

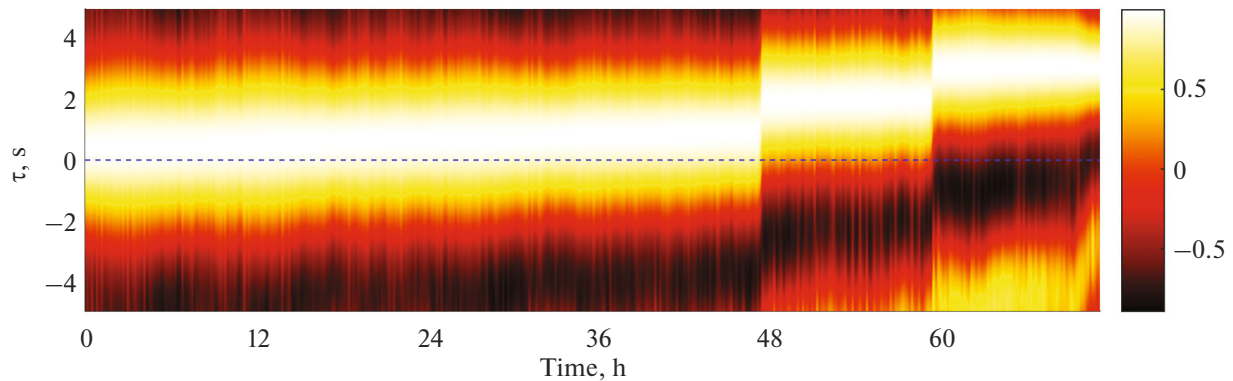


Fig. 7. Evolution of correlation function (3) for the data from sensors A and B in 20-min intervals in the first three days of measurements. The time of measurements is plotted on the horizontal axis; the time offset  $\tau$ , on the vertical axis.

#### 4. METHOD FOR RECONSTRUCTION OF DIRECTIONAL WAVE SPECTRA

Lengths of waves and directions of their motion in this work are determined using the information about delays of wave passage through the array sensors, following the known approach based on representation in the form of a Fourier series (which is sometimes called the Fourier directional method, (Young, 1994; Donegan et al., 1996)). We use the minimal configuration of the array in the form of an equilateral triangle (Fig. 2) with a side length  $\Delta l$ . The method presupposes that all three sensors simultaneously record different phases of the wave, which allows one to reconstruct information

about surface waves not shorter than  $\Delta l$  (the wavenumber is not greater than  $k = 4.2$  rad/m). For the depth  $h = 11.5 \pm 2$  m, this corresponds to a frequency region not higher than 1 Hz.

The surface displacement can be represented as a sum of harmonic waves by a set of frequencies  $\omega$  and wave vectors  $\mathbf{k} = (k_x, k_y)$ :

$$\eta(t, \mathbf{x}) = \sum_j A_j(\omega_j, \mathbf{k}_j) \exp(i\omega_j t - i\mathbf{k}_j \mathbf{x}), \quad (4)$$

where the vector  $\mathbf{x} = (x, y)$  lies in a horizontal plane. Each frequency  $\omega_j$  (which are discrete by virtue of finiteness of the time series) is in correspondence with

a unique set of values of the spectral amplitude  $A_j$  and wavenumber  $\mathbf{k}_j$  determined by the delay of wave arrival at different measurement points.

For any pair of measurement points  $(x_m, y_m)$  and  $(x_n, y_n)$ , the phase difference of the wave surface  $\Delta\varphi_{m-n}$  at an arbitrary time  $t$  can be written in the form

$$\Delta\varphi_{m-n} = \varphi_m(x_m, y_m) - \varphi_n(x_n, y_n), \quad (5)$$

where  $\varphi_m = \omega t - k_x x_m - k_y y_m$ ,  $\varphi_n = \omega t - k_x x_n - k_y y_n$  (hereinafter, we omit the subscript  $j$ ). This quantity is set equal to the difference of complex phases of Fourier transforms for the signals  $\eta_m(t)$  and  $\eta_n(t)$  at the given frequency  $\omega$ :  $\Delta\varphi_{m-n} = \arg(F_m(\omega)) - \arg(F_n(\omega))$ . For unambiguity of the determination of the phase difference  $\Delta\varphi_{m-n}$ , it is required to fulfill the abovementioned condition that the wave arriving at different sensors must be the same (then the phase difference (5) at the sensors does not exceed  $2\pi$ ). The wave vector components  $(k_x, k_y)$  for each  $\omega$  are found from the solution of a system of two algebraic equations of form (5) with constant coefficients at the unknowns specified by coordinates of the sensors and an inhomogeneous part determined by the phase difference. In our case, the pairs of array sensors A and B, as well as A and C were used; then, the matrix system of equations takes the form

$$M \begin{pmatrix} k_x \\ k_y \end{pmatrix} = \begin{pmatrix} \Delta\varphi_{B-A} \\ \Delta\varphi_{C-A} \end{pmatrix}, \quad M = \begin{pmatrix} x_B - x_A & y_B - y_A \\ x_C - x_A & y_C - y_A \end{pmatrix}, \quad (6)$$

and the solution can be written using the inverse matrix of  $M$ :

$$\begin{pmatrix} k_x \\ k_y \end{pmatrix} = M^{-1} \begin{pmatrix} \Delta\varphi_{B-A} \\ \Delta\varphi_{C-A} \end{pmatrix}. \quad (7)$$

For the array configuration presented in Fig. 2, matrix  $M$  has the form

$$M = \Delta l \begin{pmatrix} 0 & 1 \\ \cos \frac{\pi}{6} & \sin \frac{\pi}{6} \end{pmatrix}. \quad (8)$$

The  $Ox$  axis is supposed to be directed to the east; the  $Oy$  axis, to the north (Fig. 2). For the wave vector found in this way, the length  $k = |\mathbf{k}|$  and direction specified by the angle  $\theta$  with respect to the  $Ox$  axis are also defined.

The spatial spectra were constructed using data samples with a length of 512 s (the number of points in the Fourier space  $N = 2^{12}$ ) in 3-h intervals with overlapping of 50%. As a result, each discrete frequency (the frequency resolution  $1/512 \text{ s} \approx 2 \times 10^{-3} \text{ Hz}$ ) is in correspondence with an array of spectral amplitudes with certain projections of the wave vector, modulus of the wave vector, and angle which are accumulated in discrete intervals of values (the bin sorting procedure). The spectra of wavenumbers  $S(k)$ , the spectral of directional waves  $S(k_x, k_y)$ , the angular spectra  $S(\theta)$ ,

and the spatiotemporal spectra  $S(k, \omega)$  which are considered below were constructed in this way. All these functions have the meaning of spectral energy densities.

## 5. SPATIOTEMPORAL WAVE SPECTRA ACCORDING TO MEASUREMENT RESULTS

Examples of spectra  $S(k, \omega)$ ,  $S(k_x, k_y)$ , and  $S(k)$  constructed over a three-hour data interval are shown in Fig. 8. The line in the distribution of the spatiotemporal spectrum (Fig. 8a) is constructed for the theoretical curve of the dispersion relation for linear waves (1) for averaged depth  $h = 11.5 \text{ m}$ . The spectral energy of instrumental data in Fig. 8a is located considerably lower than the theoretical curve and has an almost linear character of the dependence on the wavenumber. The spatial spectrum of directional waves  $S(k_x, k_y)$  (Fig. 8b) is elongated along one direction (to the northwest) with a little spread in directions. The spectrum of wavenumbers (Fig. 8c) is concentrated in the region of unrealistically short waves  $k = 0.15 \dots 0.3 \text{ rad/m}$  (the wavelengths are 20–40 m).

The action of a flow can be a natural cause of a strong change in the dispersion relation. For the case of a homogeneous background flow  $\mathbf{U}$ , expression (1) is modified to the form

$$\omega = \sqrt{gk \tanh(kh)} + \mathbf{kU}; \quad (9)$$

therefore, the frequency of waves propagating at a small angle to the flow can considerably vary due to the Doppler effect. Ignoring the background flow in the process of spatial spectrum reconstruction can lead to an incorrect estimate of the dominant wave length and decrease in the spread of wave directions. However, significant influence on the dispersion relation for waves with a characteristic speed  $(gh)^{1/2} \approx 10 \text{ m/s}$  requires an unreal strong flow for the place of measurements.

Nonsynchronism of measurements, when the record on the sensors occurs with a time delay, can be another cause of the discrepancy between reconstructed and theoretical dispersion relations. It seems to be impossible to distinguish the natural effect of the flow from a technical problem of measurements without additional data. As described in Section 3, analysis of the behavior of correlation functions revealed accumulated desynchronization of data records due to a technical problem of sensor B; for this reason, the spatial spectra were constructed using only the time interval during first two days of measurements. At the same time, the observed position of the correlation function maximum in Fig. 7 goes beyond the expected position even in the first 48 hours. For the estimate of the propagation speed of long waves of 10 m/s, the wave passes the distance between two array sensors during 0.14 s if the discreteness of time data sequences is 0.125 s. It is well seen in Fig. 7 that the correlation function maximum by the end of the second day of measurements

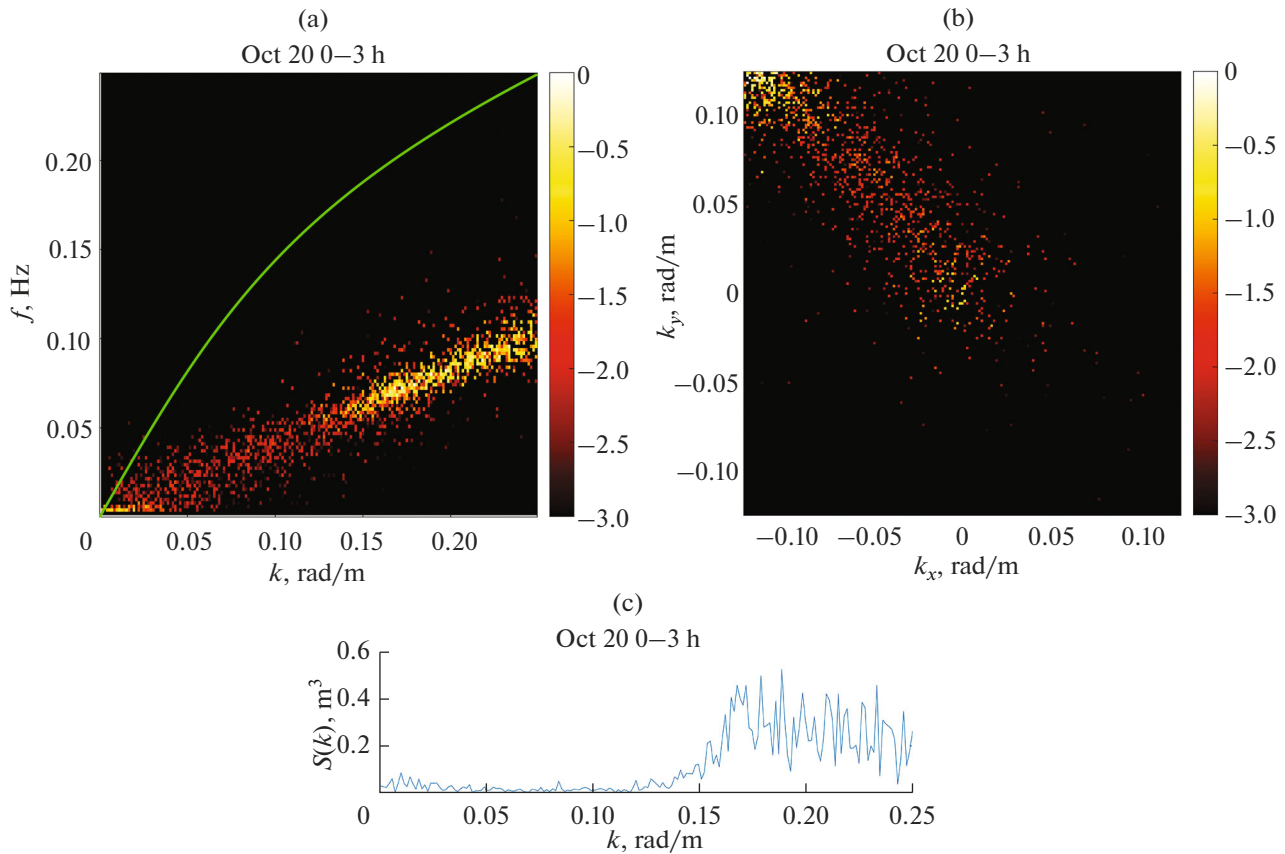


**Fig. 8.** Wave spectra calculated from data of instrumental measurements over the 3-h interval on October 2022: (a)  $S(k, \omega)$ ; the line forms the theoretical dispersion relation (1); (b)  $S(k_x, k_y)$ ; and (c)  $S(k)$ . The color in panels (a) and (b) marks decimal logarithms of the normalized quantities,  $\log_{10}(S/\max(S))$ .

moves from zero (shown in the figure by the dashed line) by an excessively large value on the order of 1 s. For this reason, the spatial spectra discussed below were constructed with introduced correction of the reference time for the record from sensor B and a constant correction to the sampling frequency of the sensor. The correcting constants were chosen from the principle of the best correspondence of the spatiotemporal spectrum  $S(k, \omega)$  to theoretical dependence (1) at the initial and final times of the 48-h record used. The data from sensor B for the corrected frequency of the device were recalculated for a frequency of 8 Hz using cubic spline interpolation.

The spatiotemporal wave spectra constructed by the corrected data are presented in Fig. 9 for four 3-h intervals in the first two days of measurements. The distribution of the spectral energy especially well corresponds to the theoretical dispersion relation in the first day (Figs. 9a and 9b). In the end of the second day, a significant deviation from the theoretical distribution is observed; attempts to noticeable reduce it using other choice of the shift of the time reference for sensor B are unsuccessful. Apparently, a certain part in the data deviation from the theoretical curve for the dispersion relation was also played by flows which were not measured independently.

Note that, as a result of correction of the time series from sensor B, a larger relative width of the angular spectra  $S(\theta)$  is observed simultaneously with better coincidence of the measurements with the dispersion relation (1); the spectra are discussed in the next section along with the picture of spatial spectra of directional waves.

In addition to energy regions with temporal and spatial scales corresponding to wind waves coming from the sea, one can distinguish in Fig. 9 low-frequency regions containing a noticeable part of energy (especially in Figs. 9a and 9b). An increase in the fraction of energy falling on large-scale wave motions in the processed data can be explained by the break of applicability conditions for the hydrostatic theory. Within the framework of the linear theory with allowance for dispersion, the characteristic scale of wave attenuation with depth corresponds to the length of the wave; therefore, long waves in the record of bottom pressure turn out to be efficiently amplified as compared to short waves. We did not reveal any manifestations of coupled nonlinear wave components not obeying the dispersion relation on spatiotemporal spectra, which is quite expectable with allowance for small nonlinearity of waves in the first two days of measurements and closeness of the conditions to the shallow-water limit.

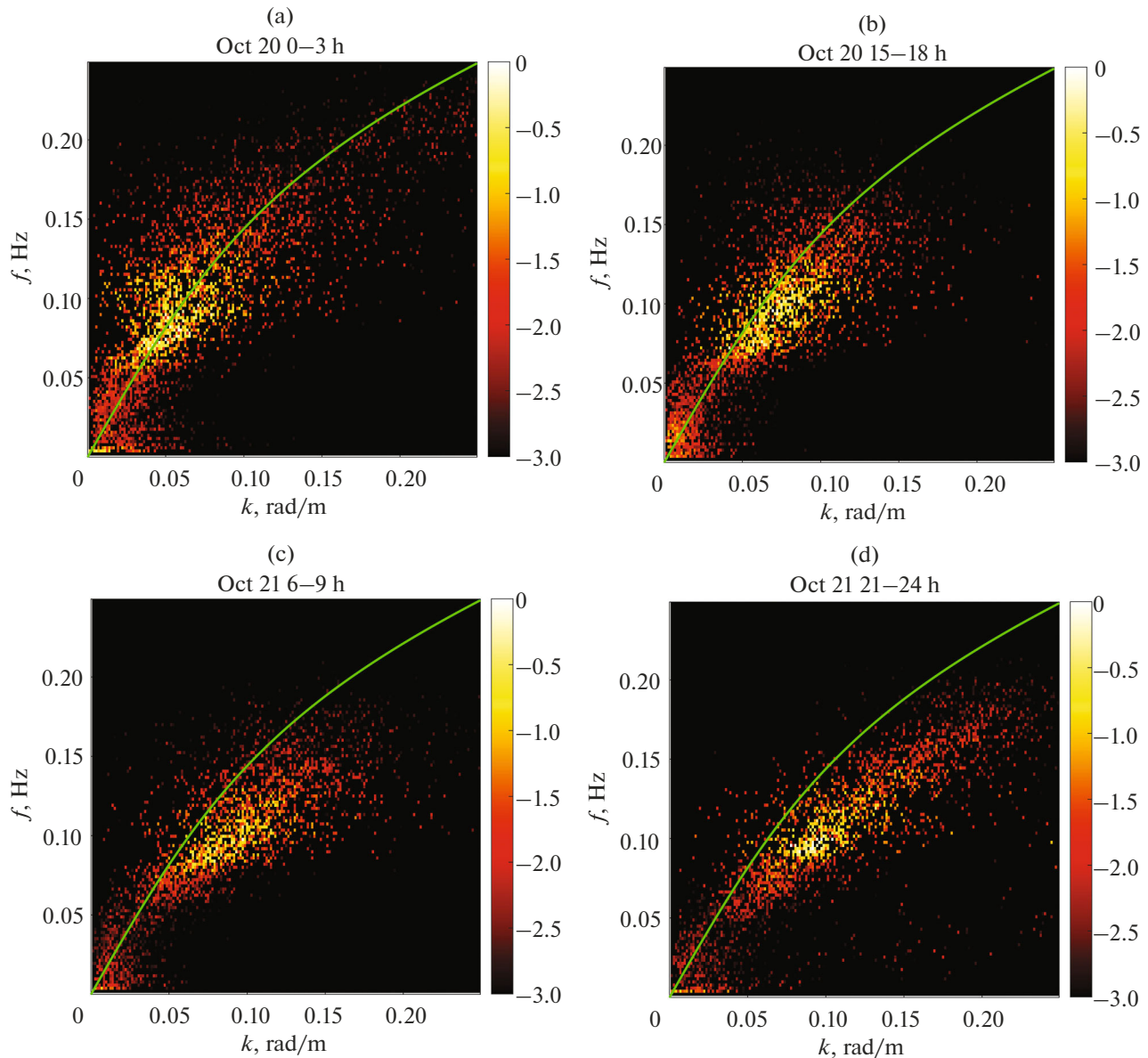


**Fig. 9.** Spatiotemporal spectra  $S(k, \omega)$  from corrected data for four 3-h time intervals in the first two days of measurements. The color marks decimal logarithms of the normalized quantities,  $\log_{10}(S/\max(S))$ ; the theoretical dispersion relation (1) is constructed by the line.

The diagrams in Fig. 10 present the evolution of the frequency spectrum of waves, as well as of the wavenumber spectrum (for corrected data) in the first two days of measurements. The spectral amplitudes are constructed in color in the linear scale. In the frequency–time spectrum (Fig. 10a), one can mention intervals with relatively intense peaks corresponding to wave periods of about 10 s (at times of 5, 14, and 28 h). Time intervals characterized by somewhat lower frequencies are also present. One can see a decrease in the frequency spectrum width by the end of the second day. The picture of the evolution of the wavenumber spectrum  $S(k)$  (Fig. 10b) in general agrees with the evolution of the frequency spectrum but looks less

clearly. A slow shift of the spectrum peak to the region of short waves is seen; however, by virtue of the performed correction of the record on sensor B, this effect can be an artifact of processing.

## 6. ANGULAR SPECTRA OF MEASURED WAVES

Based on processed data of the first two days of measurements, angular distributions of spectral density  $S(\theta)$  were constructed. They turned out to have a pronounced peak corresponding to the dominant direction of wave motion, see the examples in Fig. 11 (the blue line). Using these distributions, the wave

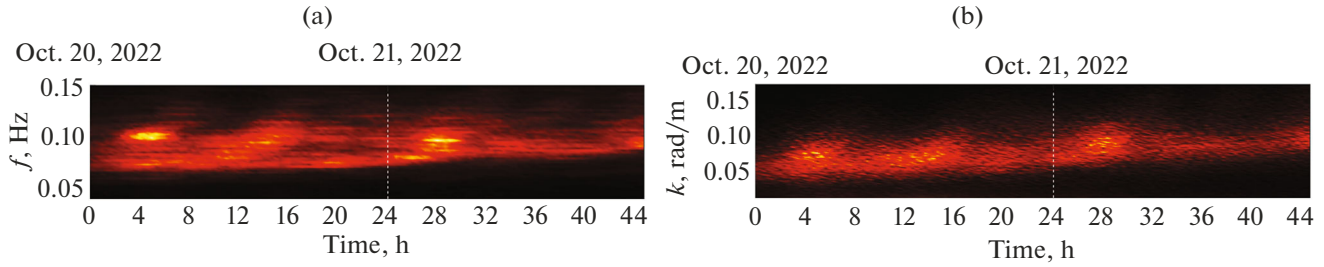


**Fig. 10.** Evolution of spectra of measured waves with respect to (a) frequencies and (b) wavenumbers in the first two days of measurements (the color marks spectral amplitudes in a linear scale).

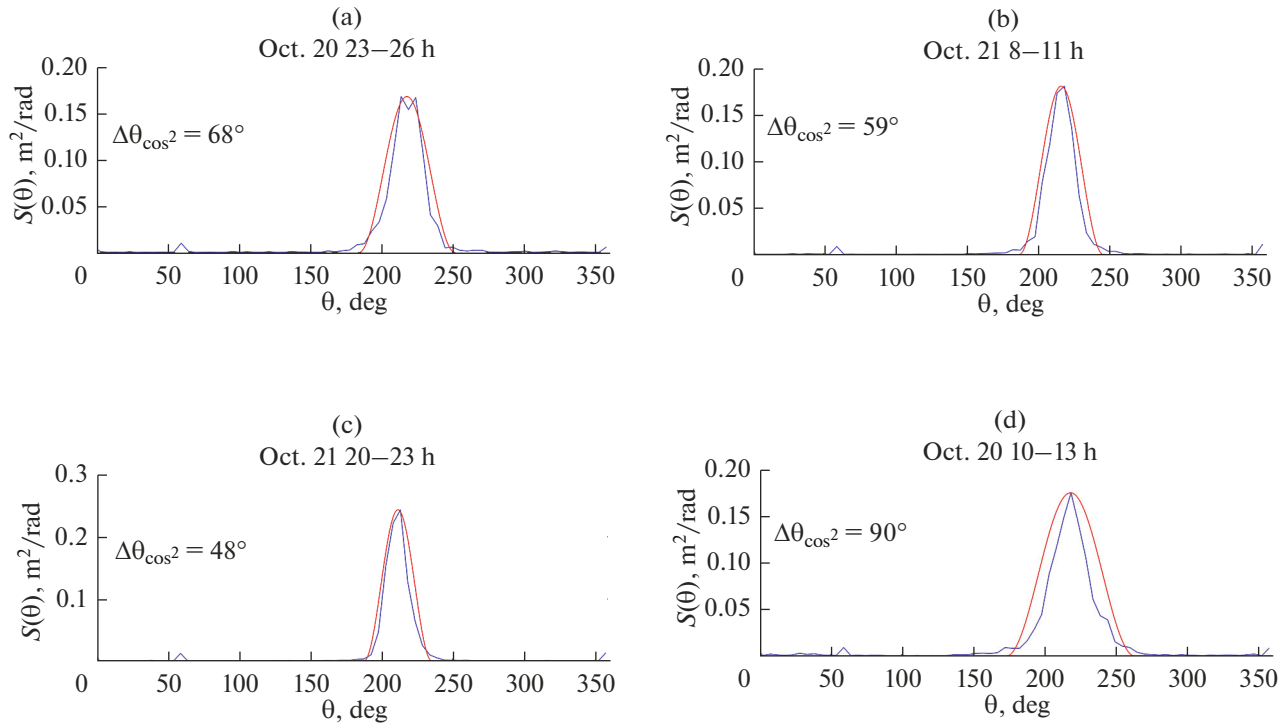


**Fig. 11.** Angular distributions of the wave spectrum from measurement data (the blue line) and parameterization (10) (the red line). Values of typical widths  $\Delta\theta_{\cos^2}$  are shown in the panels.

propagation direction as a function of time and the characteristic width of the distributions  $S(\theta)$  were determined. The experimental distributions  $S(\theta)$  were compared with the theoretical parameterization  $\cos^2$ :

$$D(\chi) = \begin{cases} \frac{2}{\Delta\theta_{\cos^2}} \cos^2\left(\frac{\pi\chi}{\Delta\theta_{\cos^2}}\right), & |\chi| \leq \frac{\Delta\theta_{\cos^2}}{2} \\ 0, & |\chi| > \frac{\Delta\theta_{\cos^2}}{2} \end{cases}. \quad (10)$$

The angle function  $D(\chi)$  describes the distribution of wave propagation directions relative to the dominant direction. For the experimental data, the wave propagation direction  $\theta_{\text{mean}}$  was determined as the “center of mass” of the periodic function  $S(\theta)$  and the

characteristic width of the angular spectrum  $\Delta\theta_{\cos^2}$  was determined by the formula

$$\Delta\theta_{\cos^2} = \frac{3}{2} \frac{\left( \int_{-\pi}^{\pi} S(\theta) d\theta \right)^2}{\int_{-\pi}^{\pi} S^2(\theta) d\theta}, \quad (11)$$

which follows immediately from (10). Variation of experimental values of the quantities  $\theta_{\text{mean}}$  and  $\Delta\theta_{\cos^2}$  in time is presented in Figs. 12a and 12b, respectively. These quantities are used to compare experimental data with the theoretical distribution (10) in Fig. 11 (the red line).

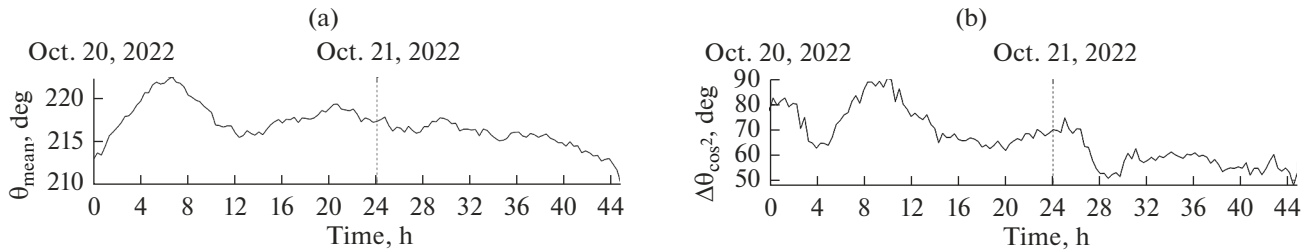


**Fig. 12.** (a) Dominant direction of waves and (b) typical width of the angular spectrum  $\Delta\theta_{\cos^2}$  during two days of measurements.

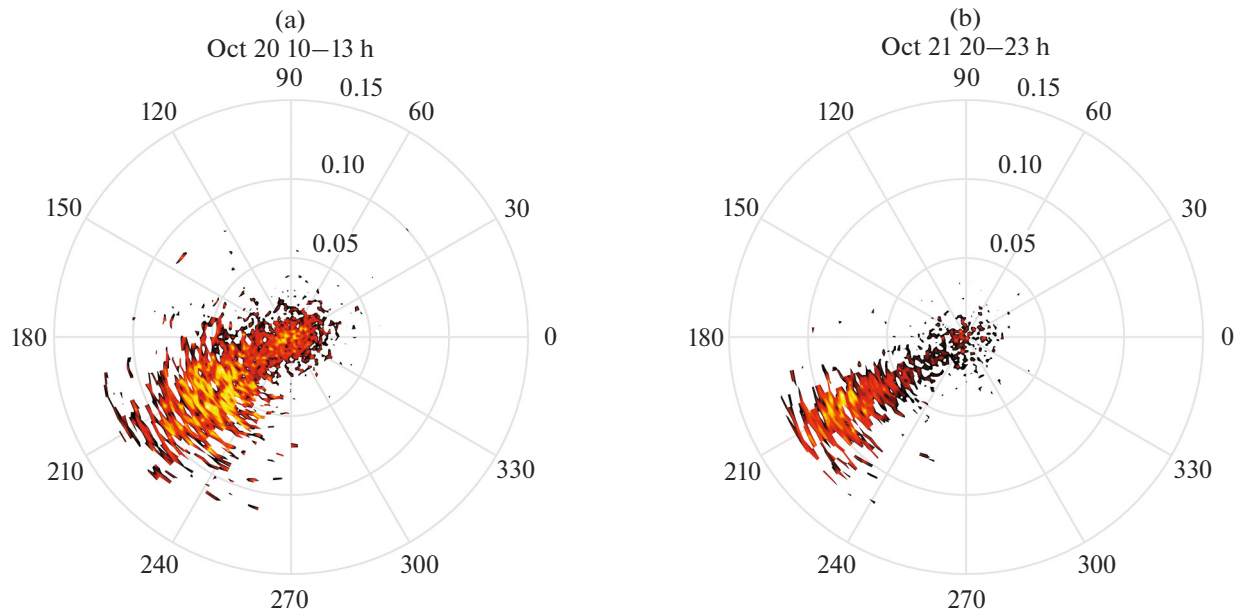


**Fig. 13.** Examples of directional wave spectra  $S(k, \theta)$  for measurements in the first two days.

As follows from Fig. 12a, the dominant direction of wave propagation during the considered 48 hours remained almost unchanged (to the southwest, which agrees with the position of the coast line at the place of measurements, see Fig. 1). The width of the angular spectrum exhibits greater variability (Fig. 12b). In general, it decreases during two days of observations; at the same time, considerable oscillations are present in the angle interval from  $50^\circ$  to  $90^\circ$ . A significant narrowing of the spread in the directions of wave propagation is observed in time intervals of the formation of more intense peaks in the frequency–time spectrum in Fig. 10a. The choice of examples of distributions  $S(\theta)$  in Fig. 11 reflects the whole range of characteristic widths of angular spectra (values of  $\Delta\theta_{\cos^2}$  determined by formula (11) are shown in the figure panels). It is seen that parameterization (10) looks well corresponding to full-scale data in all cases.

The directional wave spectra constructed in Fig. 13 yield more information about the wave energy distribution. One wave system with a dominant direction and period was observed in all examples of the distri-

butions  $S(k, \theta)$ . The pronounced energy spots in the region of very long waves (as in Fig. 13a) might be related to the break of the hydrostatic approximation, as discussed in Section 5.

## 7. INDEPENDENT ESTIMATE OF THE LOCAL DEPTHS OF THE MEASUREMENT POINT BY DATA OF THE FREQUENCY AND SPATIAL SPECTRA

Having estimates for widths of the frequency and spatial wave spectra, one may try to estimate the local depth of the measurement point. Indeed, dispersion relation (1) connects the frequency spectrum and the wavenumber spectrum, and this connection depends on the dimensionless parameter  $kh$ . Determination of relative widths of the frequency spectrum and wavenumber spectrum in terms of absolute values as  $\delta_\omega = \Delta\omega/\omega$  and  $\delta_k = \Delta k/k$  immediately yields an analytical formula for the ratio of the widths:

$$\frac{\delta_\omega}{\delta_k} = \frac{\Delta\omega k}{\Delta k \omega} \approx \frac{c_{gr}}{c_{ph}} = \frac{1}{2} + \frac{kh}{\sinh(2kh)}. \quad (12)$$

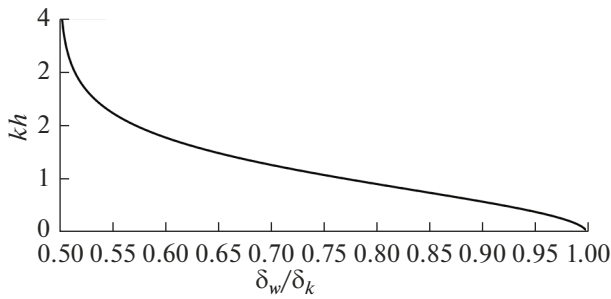


**Fig. 14.** Dependence of  $kh$  on  $\delta_\omega/\delta_k$  according to relationship (12).

Here,  $c_{ph}$  and  $c_{gr}$  are the characteristic phase and group velocities determined using (1), respectively. For relation (12) to be valid, the spectra should be relatively narrow. The quantity  $\delta_\omega/\delta_k$  as a function of  $kh$  monotonically decreases from 1 in the shallow-water limit to 0.5 in the deep-water limit. This dependence is smooth in the interval  $0 < kh < 3$  and can be used in this interval of dimensionless depths for the determination of  $kh$  by the given ratio  $\delta_\omega/\delta_k$  after reversal of relation (12), see Fig. 14.

To estimate relative widths of the spectra  $S(s)$  with the spectral variable  $s$ , we use formulas based on the standard deviation  $\delta_s$ :

$$\delta_s = \frac{1}{\bar{s}} \sqrt{\frac{\int (s - \bar{s})^2 S(s) ds}{\int S(s) ds}}, \quad \bar{s} = \frac{\int s S(s) ds}{\int S(s) ds}. \quad (13)$$

Here,  $\bar{s}$  is the mean value of the spectral variable.

The relative widths of spectra for 3-h data samples in the first two days of measurements are constructed by symbols in Fig. 15a. It is seen that they rather well fall on the straight line  $\delta_\omega = 0.73\delta_k$  (shown by the solid green line) corresponding to the dimensionless depth  $kh = 1.16$ . As judged by Fig. 4c, the parameter  $kh$  determined by the initial data gradually increased in

the first two days of measurements from 0.6 to 0.8. For comparison, the deep- (top) and shallow-water (bottom) limits are constructed in Fig. 15a by the dashed lines.

The estimate of the absolute value of the depth  $h_{sp} = kh/\bar{k}$  for the values of  $kh$  and  $\bar{k}$  determined in the way described above is constructed by symbols in Fig. 15b as a function of time. In the same figure, the depth  $h$  determined in terms of the mean displacement in 20-min samples is constructed by the black line. The result of the estimation may be called satisfactory only in the second day. At this time, the spectrum width, both in frequency and in wavenumbers (as well as in angles, see Fig. 12b), turns out to be narrower, which is favorable for the fulfillment of relation (12).

### CONCLUSIONS

In this work, wind wave regimes in Mordvinova Bay in the Sea of Okhotsk near the shore of Sakhalin Island are studied based on measurement data on variations in the bottom pressure at a depth of about 11.5 m by an array consisting of three sensors. The data array corresponds to a month of continuous measurements with a frequency of 8 Hz. The surface displacement is reconstructed using the hydrostatic theory. The significant wave height was about 20 cm during the major part of the measurement time; there was observed an episode of a storm wave with a significant height of up to 3 m. It is noted that the probability of the appearance of high (as compared to the significant height) waves decreases during a storm, which follows both from the behavior of the fourth statistical moment (the kurtosis) and from the constructed probability distributions of wave heights. The latter qualitatively agree with the theoretical Glukhovsky distribution but exhibit a significant quantitative discrepancy. This conclusion differs from the result of processing of longer measurements by individual sensors of the same construction in the same region in 2012–2015 (Kokorina et al., 2022; Slunyaev et al., 2023), where an excellent

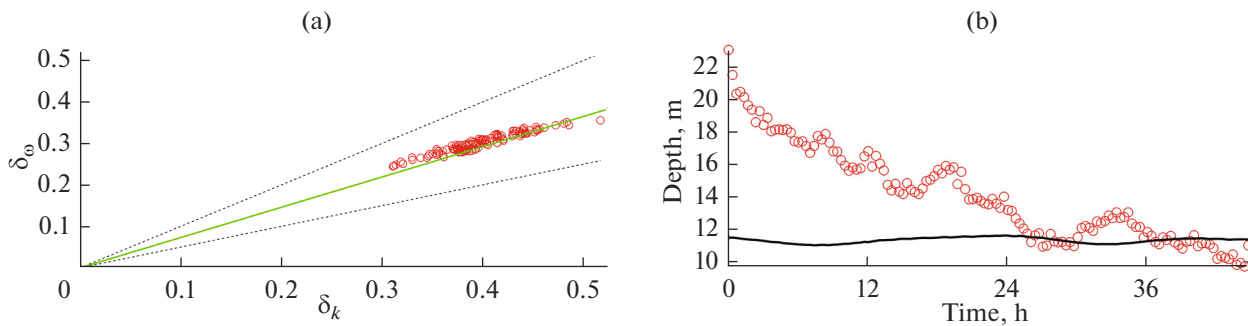


**Fig. 15.** (a) Interrelation of relative widths of the frequency and wavenumber spectra according to the measurement data (symbols). The dashed lines correspond to conditions  $\delta_\omega = \delta_k$  (above) and  $\delta_\omega = 1/2\delta_k$  (below). The solid line:  $\delta_\omega = 0.73\delta_k$ . (b) Estimate of the depth at the measurement point  $h_{sp}$  by formula (12) (symbols) and estimate of the depth  $h$  in terms of the mean in 20-min intervals of records (the solid line).

quantitative coincidence with the Glukhovsky distribution was shown for data in the ice-free period in a region of great height waves.

The spread of values of the second and fourth statistical moments determined by data from different sensors comprised in the array is estimated as 2–3% in the initial period of measurements. Then, the spread increases, which might be related to an increase in the delay of the data record by one of the sensors. To reduce the negative effect of measurement desynchronization, the spatial spectra were constructed only by data for the first two days of measurements with a correction of the time series obtained from this sensor.

The time sequences of data from the distributed array are used for reconstructing the spatial spectrum of directional waves and characteristics related to it, including the spatiotemporal and angular spectra. It is likely that such investigations of wind surface waves by bottom stations in the aspect of the measurement scheme are carried out for the first time. During two days of measurements by a synchronized array, one could observe angular spectrum distributions that are very close to the popular parameterization  $\cos^2$  (which is used, in particular, in our numerical calculations for large ensembles of nonlinear irregular waves (Slunyaev and Kokorina, 2020)) with a typical width from  $50^\circ$  to  $90^\circ$ .

It is proposed to use the relation between widths of the frequency and wavenumber spectra for estimating the local depth of the measurement point, which is theoretically supposed to allow one to determine the dimensionless depth parameter  $kh$  in the range of  $0 < kh < 3$ . This method is applied to data of full-scale measurements. The depth value reconstructed in this way turned out to be varying and it can considerably (up to by a factor of two) differ from the actual one. However, the large error can be a consequence of insufficiently well synchronization of the sensors and low intensity of waves. The conclusion about accuracy of depth reconstruction at the measurement point by this method requires additional investigations.

#### ACKNOWLEDGMENTS

We are grateful to A.V. Ermoshkin for the presented code for constructing the spatial wave spectrum by measurement data at three points of the space and D.P. Kovalev for the help in finding weather charts.

#### FUNDING

This study was supported by the Russian Science Foundation, project no. 22-17-00153.

#### CONFLICT OF INTEREST

The authors of this work declare that they have no conflicts of interest.

#### REFERENCES

- Babanin, A., *Breaking and Dissipation of Ocean Surface Waves*, Cambridge: Cambridge Univ. Press, 2011.
- Chalikov, D., Statistical properties of 3D waves simulated with 2D phase-resolving model, *Phys. Wave Phenom.*, 2023, vol. 31, pp. 114–122.
- Davidan, I.N., Lopatukhin, L.I., and Rozhkov, V.A., *Vetrovoe volnenie kak veroyatnostnyi gidrodinamicheskii protsess* (Wind Waves as a Hydrodynamic Process), Leningrad: Gidrometeoizdat, 1978.
- Donelan, M.A., Drennan, W.M., and Magnusson, A.K., Non-stationary analysis of the directional properties of propagating waves, *J. Phys. Oceanogr.*, 1996, vol. 26, pp. 1901–1914.
- Ducrozet, G. and Bonnefoy, F., Le Touzé, D., and Ferrant, P., HOS-Ocean: Open-source solver for nonlinear waves in open ocean based on High-Order Spectral Method, *Comput. Phys. Commun.*, 2016, vol. 203, pp. 245–254.
- Holthuijsen, L.H., *Waves in Oceanic and Coastal Waters*, Cambridge: Cambridge Univ. Press, 2007. <https://weatherarchive.ru/Temperature/Yuzhno-Sakhalinsk/October-2022>. <https://weatherarchive.ru/Temperature/Yuzhno-Sakhalinsk/November-2022>.
- Japan Meteorological Agency. <https://www.jma.go.jp/>.
- Kirezci, C., Babanin, A.V., and Chalikov, D., Probabilistic assessment of rogue wave occurrence in directional wave fields, *Ocean Dyn.*, 2021, vol. 71, pp. 1141–1166.
- Kokorina, A.V., Slunyaev, A.V., Zaitsev, A.I., Didenkulova, E.G., Moskvitin, A.A., Didenkulova, I.I., and Pelinovskii, E.N., Analysis of long-term measurement data on wave in Sakhalin Island, *Ekol. Sist. Prib.*, 2022, no. 12, pp. 45–54.
- Kuznetsov, K.I., Zaitsev, A.I., Kostenko, I.S., Kurkin, A.A., and Pelinovskii, E.N., Observations of rogue waves in the coastal zone of Sakhalin Island, *Ekol. Sist. Prib.*, 2014, no. 2, pp. 33–39.
- Long, C.E., *Storm Evolution of Directional Seas in Shallow Water*, Tech. Rep. CERC-1994-94-2, Vicksburg, Miss.: U.S. Army Engineer Waterways Experiment Station Coastal Engineering Research Center, 1994.
- Long, C.E. and Oltman-Shay, J.M., *Directional Characteristics of Waves in Shallow Water*, Tech. Rep. CERC-1991-91-1, Vicksburg, Miss.: U.S. Army Engineer Waterways Experiment Station Coastal Engineering Research Center, 1991.
- Lopatukhin, L.I., *Vetrovoe volnenie: Ucheb. posobie* (Wind Waves: A Teaching Book), St. Petersburg: VVM, 2012.
- Massel, S.R., *Ocean Surface Waves: Their Physics and Prediction*, Singapore: World Sci. Publ., 1996.
- Montoya, L.H. and Dally, W.R., Analysis of a 10-year record of nearshore directional wave spectra and implications to littoral processes research and engineering practice, *J. Coastal Res.*, 2016, vol. 32, pp. 1162–1173.
- Onorato, M., Waseda, T., Toffoli, A., Cavaleri, L., Gramstad, O., Janssen, P.A., Kinoshita, T., Monbaliu, J., Mori, N., Osborne, A.R., Serio, M., Stansberg, C.T., Tamura, H., and Trulsen, K., Statistical properties of directional ocean waves: The role of the modulational instability in the formation of extreme events, *Phys. Rev. Lett.*, 2009, vol. 102, p. 113502.

- Slunyaev, A.V., Contributions of nonlinear spectral components to the probability distribution of rogue waves based on the results of numerical simulation of the Euler equations, *Izv., Atmos. Ocean. Phys.*, 2023, vol. 59, no. 6, pp. 701–721.
- Slunyaev, A.V. and Kokorina, A.V., Numerical simulation of the sea surface rogue waves within the framework of the potential Euler equations, *Izv., Atmos. Ocean. Phys.*, 2020, vol. 56, no. 2, pp. 179–190.
- Slunyaev, A.V., Kokorina, A.V., Zaitsev, A.I., Didenkulova, E.G., Moskvitin, A.A., Didenkulov, O.I., and Pelinovskii, E.N., Dependence of probabilistic distributions of wave heights on physical parameters according to measurement data obtained for the Sakhalin Island, *Fundam. Prikl. Gidrofiz.*, 2023a, vol. 16, no. 3, pp. 18–29.
- Slunyaev, A.V., Pelinovskii, D.E., and Pelinovskii, E.N., Rogue waves in the sea: Observations, physics, and mathematics, *Phys.-Usp.*, 2023b, vol. 66, no. 2, pp. 148–172.
- Squire, V.A., Kovalev, D.P., and Kovalev, P.D., Aspects of surface wave propagation with and with-out sea ice on the south-eastern shelf of Sakhalin Island, *Estuarine, Coastal Shelf Sci.*, 2021, vol. 251, p. 107227.
- Wang, J., Ma, Q., Yan, S., and Liang, B., Modeling crossing random seas by fully non-linear numerical simulations, *Front. Phys.*, 2021, vol. 9, p. 593394.
- Xiao, W., Liu, Y., Wu, G., and Yue, D.K.P., Rogue wave occurrence and dynamics by direct simulations of nonlinear wave-field evolution, *J. Fluid Mech.*, 2013, vol. 720, pp. 357–392.
- Young, I.R., On measurement of directional wave spectra, *Ocean Res.*, 1994, vol. 16, p. 283.
- Zaitsev, A.I., Malashenko, A.E., and Pelinovskii, E.N., Abnormal big waves at the southern coast of Sakhalin Island, *Fundam. Prikl. Gidrofiz.*, 2011, vol. 4, pp. 35–42.

*Translated by A. Nikol'skii*

**Publisher's Note.** Pleiades Publishing remains neutral with regard to jurisdictional claims in published maps and institutional affiliations. AI tools may have been used in the translation or editing of this article.